Article

Dynamics of large scale turbulence in finite-sized wind farm canopy using Proper Orthogonal Decomposition and a novel Fourier-POD framework

Tanmoy Chatterjee [1,†,‡] and Yulia T. Peet [2,‡]

[1] Arizona State University; tchatte3@asu.edu
[2] Arizona State University; ypeet@asu.edu
* Correspondence: tchatte3@asu.edu

Abstract: Large scale coherent structures in atmospheric boundary layer (ABL) are known to contribute to the power generation in wind farms. In the current paper, we perform a detailed analysis of the large scale structures in a finite sized wind turbine canopy using modal analysis from three dimensional proper orthogonal decomposition (POD). While POD analysis sheds light on the large scale coherent modes and scaling laws of the eigenspectra, we also observe a slow convergence of the spectral trends with the available number of snapshots. Since the finite sized array is periodic in the spanwise direction, we propose to adapt a novel approach of performing POD analysis of the spanwise/lateral Fourier transformed velocity snapshots instead of the snapshots themselves. This methodology not only helps in decoupling the length scales in the spanwise and the streamwise direction when studying the energetic coherent modes, but also provides a detailed guidance towards understanding the convergence of the eigenspectra. In particular, the Fourier-POD eigenspectra helps us illustrate if the dominant scaling laws observed in 3D POD are actually contributed by the laterally wider or thinner structures and provide more detailed insight on the structures themselves. We use the database from our previous large eddy simulation (LES) studies on finite-sized wind farms which uses wall-modeled LES for modeling the Atmospheric boundary layer laws, and actuator lines for the turbine blades. Understanding the behaviour of such structures would not only help better assess reduced order models (ROM) for forecasting the flow and power generation but would also play a vital role in improving the decision making abilities in wind farm optimization algorithms in future. Additionally, this study also provides guidance for better understanding the POD analysis in the turbulence and wind farm community.

Keywords: proper orthogonal decomposition; wind farms; eigenspectra; counter-rotating roll cells

---

1. Introduction

Wind farms in atmospheric boundary layer (ABL) pose a complex dynamical system with turbulent phenomenology occurring at multiple length scales, mainly due the interaction of atmospheric boundary layer turbulent eddies [1] and the turbulence generated by the wind turbine wakes [2–4]. These interactions are manifested not only in the small scale structures (of the order or smaller than the turbine rotor diameter) but also in the large scale structures (one or two orders of magnitude larger than the turbine rotor diameter) [5]. In the current paper, we are concerned towards the understanding of these large turbulent structures which arguably can serve as mediators to the generation of large scale motions or very large scale motions [6] (LSM's or VLSM's) which has significant contribution to wind farm power [4,7]. Several researchers have shown before that large scale counter-rotating roll cell structures are formed in atmospheric boundary layer [8–11], and wind farms in ABL modulate such structures in and around the turbine rotors [12–14]. Proper orthogonal decomposition aka POD [15–17], has been popularly used by the community to perform detailed analysis of these large scale roll structures [15], because of its inherent nature to "rank"

Preprints (www.preprints.org) | NOT PEER-REVIEWED | Posted: 26 February 2020 doi:10.20944/preprints202002.0390.v1

Peer-reviewed version available at *Energies* **2020**, *13*, 1660; doi:10.3390/en13071660

the coherent turbulent eddies based on their kinetic energy content (POD eigenvalues). In the current manuscript we are primarily interested in the POD analysis of a finite-sized wind farm where the flow is heterogeneous in the streamwise direction. Finite sized wind farms have multiple applications, e.g., fundamentally from understanding the entrance region of very large wind farms [18] without restrained by computational expense. These finite sized turbine arrays also find their place in utility scale farms e.g., in a distributed wind setup aimed for powering rural or remote sub-urban community [19]. One of the key problems, in the snapshot-based POD analysis [20–22] (more popular because it is computationally cheap), is that the snapshots need to be quite far spaced (more than three flow though times apart), such that the snapshots are linearly independant of each other for the generation of the correlation matrix in POD, and hence capture the large scale structures/modes (having large decorrelation times). Restrained by the computational expense, the number of snapshots in such a case involving finite sized wind farm canopy will be quite limited, which will detrimentally impact the scaling and the convergence of the POD eigenspectra. Previous work by turbulence/wind community have not addressed this issue explicitly [23]. This problem was circumvented by performing the analysis on a periodic wind farm [15]. In this way even though very few distant spaced (3 flow through times apart) snapshots are generated by solving the Navier-Stokes equation, the number can be artificially amplified by "shifting" the snapshot data across the streamwise and spanwise distance between the turbines. The shifting method only works if the wind farms are arranged in a completely matrix setting ($n_x \times n_y$ turbines) in a horizontally periodic framework. In this case the total number of snapshots generated for POD would be $n_x n_y$ times the snapshots obtained from simulations. In the finite sized wind farm, as in the current manuscript, due to the heterogeneity of the farm layout and the geometry of the domain, such shifting is not possible, and at most we can increase the number of snapshots by two times by reflecting the data across xz plane of symmetry passing through the middle row of turbines. Thus the data from finite-sized wind farm simulation serves as a perfect candidate for performing such POD analysis studies. As we will see later, that this creates a limitation on the total number of snapshots we can generate that impacts negatively on the convergence of the POD eigenspectra. Additionally after performing detailed analysis of the eigenspectra and understanding the dynamics of the 3D eigenmodes, we adapt a Fourier-POD (FPOD) based framework for better understanding of the eigenspectra (most importantly their convergence) as well as the modes. In this methodology, we perform POD analysis of laterally/spanwise fourier transformed snapshots rather than the 3D snapshots themselves. As will be discussed in the subsequent section, we see that the FPOD modes can provide better insights to the scaling laws of the eigenspectra as well as illustrate on the turbulent structures which contribute to the problem of "slower convergence" of the spectra. Ideas for computing POD with a similar spirit exists in the literature, e.g., spectral POD (SPOD) by Towne and coworkers [24], where the temporal fourier transform of the correlation function is used for POD eigen decomposition problem in order to understand the modal frequency content. Towne and coworkers also-showed the connection between SPOD and dynamic mode decomposition (DMD) [25]. Hamilton and coworkers [26,27] have introduced methodologies like dual POD as well as 2D-POD at each streamwise location in an effort to understand the streamwise dependencies of the coherent structures for wind farms. Glegg and Devenport [28] have also shown that for problem involving turbulence-acoustics interference, POD can be performed in combination of linear stochastic estimator in the homogeneous direction (space or time for homogeneous/stationary flows) to describe flows and that such analysis requires less modes for flow representation than the conventional 3D POD. The methods described above have utilized POD such that additional information of length scale dynamics/ decoupling streamwise and spanwise length scales are possible. The concept of Fourier-POD itself is not uncommon in the turbulence community and can be found in many canonical flows having a homogeneous direction, the most recent being Rayleigh Benard convection [29,30]. Contrary to the previous methods, the FPOD methodology (operated on complex two dimensional structures) and its novelty in the current work lies in its introduction to solely gain physical insight to the convergence of the 3D eigenspectra and additionally showing a comparison of the reconstructed

POD modes from FPOD modes with the 3D POD modes. Additionally, FPOD also helps us decouple length scales of the energetic eddies based on the spanwise and streamwise direction of the flow. Decoupling of length scales create more information of the turbulent large scale structures present in the wind farms in atmospheric boundary layer which can be used as insights to understanding eigenspectra convergence and turbulent structures.

The paper is organized as follows. First we briefly discuss the numerical setup with regards to the large eddy simulation (LES) framework used for the wind farm simulations. Specifically, we also discuss about the three dimensional proper orthogonal decomposition (method of snapshots) used in the context of wind turbine simulations followed by analysis of the 3D results. We highlight certain drawbacks in the method and in order to gain more insight to those drawbacks we introduce the 2D Fourier-POD methodology accompanied by the results. Finally we conclude highlighting the merits of 2D Fourier-POD methodology in understanding the physics of wind farm compared to its 3D POD counterpart.

2. Numerical Setup

The database for the finite sized wind farm have been obtained from spectral element simulations in LES carried out in our previous work [5,31,32]. In particular, we use the open-source exponentially accurate spectral element code Nek5000 [33,34] for setting up the LES simulation. Nek5000 solves the incompressible Navier-Stokes equation in a variational/weak formulation with tessellating the domain into 3D hexahedral elements. The variables, velocity, pressure etc., are expanded as higher order Legendre polynomials within each element and the gridpoints where the polynomials are defined are essentially the roots of the polynomials or Gauss-Lobatto-Legendre (GLL) points (Gauss-Lobato (GL) points for pressure, in the current formulation).

The domain consists of a 3×3 wind turbine array (WT) in a realistic inflow-outflow [31,35] setup, and hence the turbine array layout is finite-sized. The inter-turbine streamwise and spanwise distances are $7d$ and $3d$ respectively. The wind turbine rotors in the finite sized array, d is set to be 20% of the ABL thickness and the hub-height being $z_h = d$. Such setup of hub-heights are consistent with the wind-tunnel laboratory scale wind turbine tests carried out in the past [7,36]. The vertical height of the domain is $5d$. The LES framework involves wall-modeled large eddy simulation with the subgrid scale closure designed as algebraic wall-damped Mason and Thompson model [37–39] and the bottom wall boundary condition prescribed as wall-stress (corresponding to the log-law of the wall). For validation of neutral ABL and wind farm simulations in spectral elements, please refer to the authors' previous work [5,40]. The wind turbines are modeled as actuator-line models [41–44]. Moreover, the finite-sized layout is inherently heterogeneous due to the streamwise growth of the internal boundary layer, wake impingement effects etc. The top boundary condition of the finite-sized wind farm array is "symmetry" or no mass transport in nature which mimics an inversion layer as in a conventionally neutral boundary layer [45,46]. For the current setup, the *artificial inversion layer* is 5 times the hub-height/rotor diameter of the turbines and can be thought of as low-lying [45]. From the perspective of canopy turbulence, it is apparent that the ABL above the wind turbine canopy is essentially the "canopy sub-layer" (vertical domain size $5d/5z_h$). (The canopy sublayer, is where the turbulent eddy effects of the canopy are still felt and is roughly 5 times the canopy height or even larger, see [47–49] for details of recent canopy/roughness sublayer fundamentals). We further illustrate the schematic of the three-dimensional layout in Figure 1a and supported by a typical snapshot of fluctuating streamwise velocity at hub-height (Figure 1b), where the multiscale feature of ABL-turbulence around the rotor regions are evident. Table 1 shows the specification of the domain size of the wind turbine array as well as the precursor neutral ABL which is concurrently simulated to generate inflow conditions [31,32]. Additionally, the grid counts and the average normalized grid sizes for the farm layout as well as neutral ABL (turbulent scales fed to the inflow) can be found in Table 2. This illustrates that the smallest resolved length scales is an order of magnitude smaller than the turbine rotor size, d. Note, here that the definition of lengthscales or wavelength resolved is

Peer-reviewed version available at Energies 2020, 13, 1660; doi:10.3390/en13071660

Case	Geometry	$N_x^e \times N_y^e \times N_z^e$	Grid points
Neutral ABL	$10\pi d \times 5\pi d \times 5d$	$30 \times 20 \times 24$	5.06×10^6
WT Array	$15\pi d \times 5\pi d \times 5d$	$48 \times 32 \times 24$	1.281×10^7

Table 1. Details of the computational grids for the precursor ABL and the wind turbine array domain. N_η^e is the number of spectral elements in the η direction. 8 GLL nodes (Legendre polynomial order 7) have been used per element per Cartesian direction

	Neutral ABL			WT Array		
Direction	$\lambda_{\eta,res\,\max}$	$\lambda_{\eta,res\,\min}$	$\overline{\lambda}_{\eta,res}$	$\lambda_{\eta,res\,\max}$	$\lambda_{\eta,res\,\min}$	$\overline{\lambda}_{\eta,res}$
x	$0.2992d$	$0.2992d$	$0.2992d$	$0.3366d$	$0.0944d$	$0.2804d$
y	$0.2240d$	$0.2240d$	$0.2240d$	$0.3316d$	$0.0358d$	$0.1402d$
z	$0.0596d$	$0.0596d$	$0.0596d$	$0.0942d$	$0.0476d$	$0.0596d$

Table 2. Maximum, minimum and average wavelengths captured, for the ABL and the wind turbine array domain. d is the turbine rotor diameter.

based on the Nyquist limit of the coarsest grid size (twice the coarsest grid size). For more details of how the grid sizes were defined, See [5,43]. From table 1 it is apparent that the precursor neutral ABL has a much uniform distribution of grids compared to the wind turbine (WT) domain. This is primarily because of the fact that the WT domain grids were build on the top of ABL domain, with grid refinements around the turbine rotors ($\sim$ 30 gridpoints per actuator line blade) for capturing the wake turbulence accurately [31,35,43,50].

The number of snapshots obtained from the simulations is 3285, which are spaced $1/5T_e$ apart ($T_e = 15\pi d/U_\infty$ is the flow-through time). Since, the domain/layout is symmetric about $y = 2.5\pi d$, we created $2 \times 3285 = 6570$ snapshots by reflecting /shifting the snapshot data about xz plane at $y = 2.5\pi d$ (similar to the shifting method by Verhulst et al. [15]).

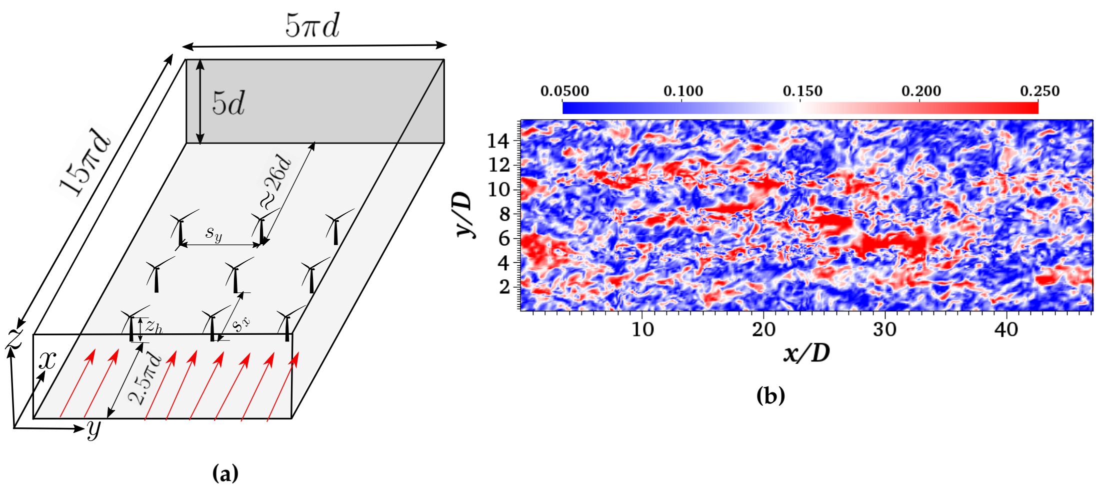

Figure 1. (a) Schematic of the 3×3 wind turbine array. (b) Normalized streamwise fluctuation velocity, u'/U_∞ at hub-height location, $z = z_h = d$. Red arrow: inflow condition from precursor neutral ABL.

Preprints (www.preprints.org) | NOT PEER-REVIEWED | Posted: 26 February 2020 doi:10.20944/preprints202002.0390.v1

Peer-reviewed version available at *Energies* **2020**, *13*, 1660; doi:10.3390/en13071660

3. Results

3.1. 3D POD – Method of Snapshots

The POD analysis was carried out using the *method of snapshots* [20] developed in the spectral element code Nek5000. The 3D velocity vector field is represented as $\boldsymbol{u}(\boldsymbol{x},t) \equiv u_i(x,y,z,t)\ \forall i = 1,\ldots,3$. Here, $u_i(x,y,z,t) \in \Omega(\mathbb{R}^3,[0,\infty) \cap L_2(\mathbb{R}^3))$. ($\mathbb{R}^3$ is the 3D real space, $L_2(\mathbb{R}^3)$ is the L_2 or energy norm in the 3D real space.) The velocity field can be decomposed into a set of orthonormal basis functions $\boldsymbol{\varphi} \in V \equiv \Omega(\mathbb{R}^3 \cap L_2(\mathbb{R}^3))$.

$$\boldsymbol{u}'(\boldsymbol{x},t) = \sum_{j=0}^{\infty} a_j(t)\boldsymbol{\varphi}_j(\boldsymbol{x}) \tag{1}$$

where the turbulent velocity fluctuation field $\boldsymbol{u}'(\boldsymbol{x},t) = \boldsymbol{u}(\boldsymbol{x},t) - \overline{\boldsymbol{u}}(\boldsymbol{x})$, and $\overline{\boldsymbol{u}}(\boldsymbol{x})$ is the time average of the velocity field. $(\varphi_i,\varphi_j) = \delta_{ij}\ \forall i,j$. The POD problem can be cast as a constrained variational problem, with the minimization of the objective function $\mathfrak{J}(\boldsymbol{\varphi}) = \langle|(\boldsymbol{u}',\boldsymbol{\varphi})|^2\rangle_T - \Lambda(||\boldsymbol{\varphi}||^2 - 1)$, $\langle\rangle_T$ is a temporal averaging procedure. A necessary condition of the extrema dictates that the functional derivative vanish for all variations $\boldsymbol{\varphi} + \varepsilon\boldsymbol{\psi} \in V,\ \varepsilon \in \mathbb{R}$, .i.e.,$\frac{d}{d\varepsilon}\mathfrak{J}(\boldsymbol{\varphi}+\varepsilon\boldsymbol{\psi})|_{\varepsilon=0} = 0$. The method of snapshot is an approximation to the solution of $\frac{d}{d\varepsilon}\mathfrak{J}(\boldsymbol{\varphi}+\varepsilon\boldsymbol{\psi})|_{\varepsilon=0} = 0$ [22] using temporal correlation instead of spatial correlation. Mathematically, the POD method of snapshots [20] of the velocity field dataset arises when solving for the projection of the dataset $\mathbf{P}_r : V \mapsto V_r$ of fixed rank r, minimizing the error $\sum_{j=0}^{N_t-1} ||\boldsymbol{u}_j' - \mathbf{P}_r\boldsymbol{u}_j'||^2$ in the least-square sense with the constraint $||\varphi|| = 1$ ($||.||$ is the norm corresponding to the inner product $(,) \in V$). The temporal snapshots of the velocity field $\boldsymbol{u}(\boldsymbol{x},t_j)\ \forall j = 1,\ldots,N_t$ have been written as $\boldsymbol{u}_j$ in the error expression for brevity. The projection $\mathbf{P}_r$ can be written as

$$\mathbf{P}_r\boldsymbol{u}_m' = \sum_{j=0}^{r-1}(\boldsymbol{\varphi}_j,\boldsymbol{u}_m')\boldsymbol{\varphi}_j = \sum_{j=0}^{r-1} a_j(t_m)\boldsymbol{\varphi}_j(\boldsymbol{x}), \quad r \le N_t \tag{2}$$

The correlation matrix in indicial notation can be obtained from the inner product of the snapshots and is given as

$$C_{mn} = \frac{1}{N_t}(\boldsymbol{u}'(\boldsymbol{x},t_m),(\boldsymbol{u}'(\boldsymbol{x},t_n)) \tag{3}$$

This method ensures that the eigenvalue problem arising is independent of the size of V which is equal to $\Omega(\mathbb{R}^{3k})$ (k: number of coordinates in $\boldsymbol{u}(\boldsymbol{x},t)$ at discrete grid points). In the eigenvalue problem in Equation 4 below, Λ is the eigenvalue corresponding to the turbulent kinetic energy and $\boldsymbol{v}$ is the eigenvector.

$$[\boldsymbol{C}]\boldsymbol{v} = \Lambda\boldsymbol{v} \tag{4}$$

The POD eigenmode can be constructed from the eigenvalues and eigenvectors as

$$\boldsymbol{\varphi}_k(\boldsymbol{x}) = \sum_{j=0}^{N_t-1} b_k(t_j)\boldsymbol{u}'(\boldsymbol{x},t_j) \tag{5}$$

Preprints (www.preprints.org) | NOT PEER-REVIEWED | Posted: 26 February 2020 doi:10.20944/preprints202002.0390.v1

Peer-reviewed version available at *Energies* **2020**, *13*, 1660; doi:10.3390/en13071660

for some coefficients b_k. Using equation 2 for $\boldsymbol{u}'(\boldsymbol{x}, t_j)$, equation 5 can be expanded as

$$\begin{aligned}\boldsymbol{\varphi}_k(\boldsymbol{x}) &= \sum_{j=0}^{N_t-1} b_k(t_j) \sum_{l=0}^{N_t-1} a_l(t_j)\boldsymbol{\varphi}_l(\boldsymbol{x}) \\ &= \sum_{j=0}^{N_t-1}\sum_{l=0}^{N_t-1} b_k(t_j)a_l(t_j)\boldsymbol{\varphi}_l(\boldsymbol{x})\end{aligned} \tag{6}$$

Since, $(\boldsymbol{\varphi}_k, \boldsymbol{\varphi}_l) = \delta_{kl}$, it is straightforward to see from equation 6 that $b_k(t_j)a_l(t_j) = \delta_{kl}/N_t \;\; \forall j$. It is important to note, that Parseval's identity can be applied in POD (orthonormal basis functions) which from the inner product (taken in spatial domain, defined in V) gives rise to $||\boldsymbol{u}'(\boldsymbol{x}, t)||^2 = \sum_{j=0}^{N_t-1} a_j(t)^2$, and hence $\langle a_j(t)a_k(t)\rangle_T = \Lambda_j\delta_{jk} \;\; \forall j = 0, \ldots, N_t - 1$. Thus, since $b_k a_l = \delta_{kl}/N_t$, the coefficient b_k can be defined as $b_k = \frac{a_k}{\Lambda_k N_t}$. Also the eigenvector $v_k = \frac{a_k}{\sqrt{\Lambda_k N_t}}$ is consistent with the orthonormality of $\boldsymbol{\varphi}$.

In this section we present the results obtained from the POD analysis of a finite-sized wind turbine array. Unless otherwise mentioned, the results (also shown in the plot labels) have been normalized with the free-stream velocity scale, U_∞ and rotor diameter d as deemed necessary. The snapshots for the layout are each $T_e/5$ (T_e is the flow through time) snapshots apart, which are much frequent than the snapshots "$3T_e$ apart" as reported in Ref. [15]. This essentially means that the current POD analysis were carried out in the framework of "smaller time scales". The snapshots $\sim 3T_e$ apart in the previous literature [15] in the context of asymptotic wind farms ensure that the temporal autocorrelation of the velocities completely decay to zero. In the current manuscript we resort to snapshots separated by time $T_e/5$, when the velocity correlations are roughly ~ 0.2. However, we have also used snapshots which are $2T_e/5, 3T_e/5 \& 4T_e/5$ times apart to test the convergence of the eigenspectra. The time extent of $600T_e$ has been used for the analysis of the LES database. Note, that during convergence study, we have chosen to keep the time extent of the database for POD analysis be fixed and only varied the time spacing between the two snapshots. Ref. [15] performed POD analysis on periodic wind farm layout, and hence after generating a set of snapshots, $3T_e$ apart, artificially increased the number of snapshots by an order of magnitude by exploiting the stationarity of the flow and the large scale statistical symmetry of the flow around every turbines in the streamwise and spanwise direction (method of "shifting"). Figure 2a shows the normalized eignenspectra of the finite-sized farm layout compared with the spectra of a periodic 8×6 array with domain size $20\pi d \times 10\pi d \times 10d$ (with one shifting using spanwise symmetry) performed by the current authors as well as a periodic 4×6 array with domain size $10\pi d \times 10\pi d \times 10d$ (with 4 shifting) by Verhulst et al [15]. Note, the data of the 8×6 array reported by the current authors were generated and benchmarked in [5]. Additionally, we also illustrate the convergence behaviour of the eigenspectra for the finite sized farm in Figure 2b. Note, instead of comparing the eigenvalues for different POD problems λ_m, we compare the normalized eigenvalues λ_m/λ_1 (m is the number of mode), which ensures better convergence of the scaling trends.The current convergence plots were shown for a POD computed for a same time extent of $600T_e$, but the snapshots were spaced for different fractions of flow-through times apart. However, similar trends in convergence can be observed when performed with the POD for fixed spacing of the snapshots ($T_e/5$) and progressively adding more snapshots with each case (results not added for brevity). The eigenspectra and their convergence trends clearly indicate the following features, i) *convergence is observed by increasing N_t, the number of snapshots*, ii) *with increasing number of snapshots, the scaling law of the modes for $m > 10$, clearly change from $m^{-0.5}$ [16] to $m^{-0.8}$ which is extremely close to $m^{-0.9}$ as observed by the periodic wind farms in [15]*. Additionally we can also comment that obtaining the convergence of $m^{-0.9}$ scaling law is primarily dependent on the number of snapshots rather than the spacing of the snapshots. Incidentally, a similar scaling law $m^{-1.2}$ was also observed for 2D POD eigenspectra performed at different streamwise locations of wind turbine array by Hamilton and coworkers [27]. We hypothesize that with increasingly more number of snapshots, the scaling law for modes $m > 10$, should approach $m^{-0.9}$. However, restrained by the bottleneck of the computational expense we cannot add further snapshots from simulation or take advantage of the symmetric shifting to generate more "artificial" snapshots. Consequently, in order to gain more insights on the scaling law of the eigenspectra and their convergence, we propose a different methodology based on Fourier-POD analysis, which essentially deals with the POD of the snapshots of the lateral/spanwise Fourier transformed velocities for different wavenumbers instead of the 3D snapshots themselves. We provide a dedicated section (Section 3.2) for introducing the mathematical formulation and the results and insights of the FPOD analysis, but for now we continue our discussion related to the results of the 3D POD analysis.

Figure 3 shows the frontal (yz plane) picture of the POD modes for the first 8 eigenvalues. In particular, the figures illustrate the colour contours of the streamwise modes overlayed on the top of in-plane (vertical, spanwise) modes represented as vectors. The modes clearly manifest circulatory features, reminiscent of the counter-rotating roll-cell structures and the downdrafts and updrafts of these circulations coincide with the positive (higher energy) and negative (lower energy) streamwise modal structures. The number of roll-cells observed in the layout is related to the modes and hence the eigenvalues/kinetic energy of the flow domain. Figure 4 gives a 3D perspective to the circulatory roll-cell features we discussed above, in particular, mode $k = 0$. The isosurface of the streamwise velocity modes indeed shows the long counter rotating roll-cell feature spanning the whole domain. This is corroborative of the fact that these roll-cell features are a phenomenology of the atmospheric boundary layer turbulence [9,15]. The streamtube picture depicted in Figure 4b further illustrates the three-dimensional nature of the large-scale structure manifested by the most dominant POD mode. The three sets of the circulatory features depicted by the streamtubes are formed in and around the 3 columns of the turbines.

In order to get a better understanding of how the wind farm modulates these large scale structures we take a closer look at the streamwise variation of the modes in Figure 5 illustrated as the contour plots of the POD mode velocity magnitude. As we will see later that the streamwise plots also assist us to make a one-to-one comparison with the Fourier-POD modes discussed in the subsequent sections. We observe the streamwise (almost) homogeneous streaks which are essentially footprints of the roll-structures for lower modes. Interestingly, in those footprints we can observe "wake like features" which are clearly manifestation from the wind turbine array. For modes $m < 3$, we observe that the wake like features (velocity-deficits) extend for scales $\sim 7d$ (inter-turbine distances) embedded in the roll-cell footprints. Particularly, for mode $m = 3$, the "wake" footprints can be conspicuously observed with high-velocity regions near the turbine wake rotors and is a clear manifestation of the modulation of the flow structure modes by wake-turbulence. This is reminiscent of the generation of turbulent kinetic energy at the wakes due to vertical entrainment at the inner layer. The mode $m = 3$ is a clear example of the mode that is entirely due to wind-farm-ABL interactions and would not form in a pure ABL case. Apart from the rolls, at higher modes ($m \gtrapprox 7$), we also observe large structures starting from the wall and inclined at an angle of $15 - 20$ degrees [51,52]. We believe that these inclined structures are footprints of clusters of hairpin vortices which together forms the framework of "attached eddies" [53,54].

The dynamics or the temporal variation of the modes are imprinted in the projection coefficients illustrated in Figure 6. Since, $||\boldsymbol{u}'(\boldsymbol{x},t)||^2 = \sum_{j=0}^{N_t-1} a_j(t)^2$, as explained in the mathematical formulation owing to Parseval's theorem, the coefficients $a_k(t)$ bear the temporal/dynamical footprints of the kinetic energy contained in the velocity fluctuations. Expectedly, the projection coefficients corresponding to the lower order modes $(0 - 3)$ show low frequency fluctuations compared to the projection coefficients corresponding to modes 4 or more, indicating the fact that larger scales of motion are supposedly made by eddies of larger time scales. Additionally, the power spectral density of the projection coefficients

Preprints (www.preprints.org) | NOT PEER-REVIEWED | Posted: 26 February 2020 doi:10.20944/preprints202002.0390.v1

Peer-reviewed version available at Energies 2020, 13, 1660; doi:10.3390/en13071660

(in frequency space) of the large scale modes ($k < 5$) manifest a f^{-3} scaling law (f is the frequency) which has been attributed to the phenomenon of "merging of eddies" by previous literature [55,56] (Figure 6c). Note, we start observing the $f^{-5/3}$ law for modes $m = 9$ (and higher) manifesting energy cascade. Consequently, it can be argued that the low-time scale dynamics of the structures comprising of the lower 3D POD modes are predominantly governed by merging of eddies.

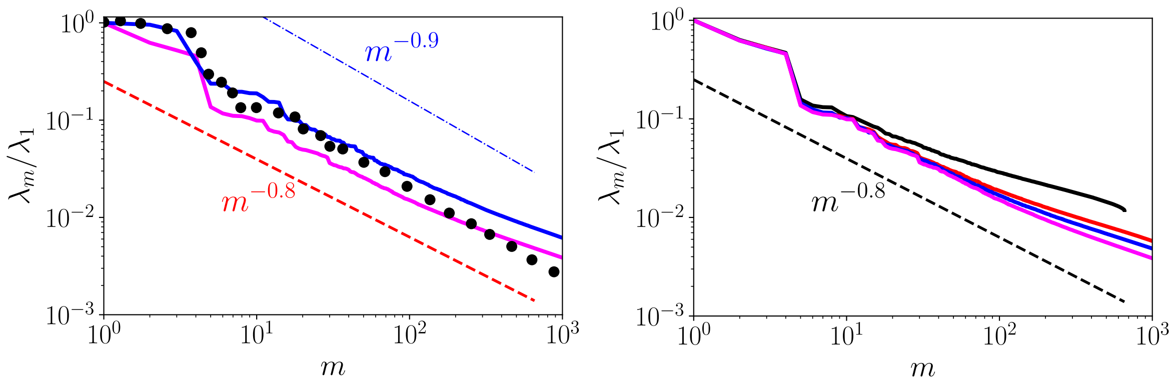

(a) **(b)**

Figure 2. (a) Eigenvalue spectrum normalized by the first eigenvalue (highest energy)) for different wind turbine layout. Blue – periodic wind farm (asymptotically infinite) with 8×6 array [5], Magenta – current finite sized wind farm (3×3 array, solid magenta). Black circle – periodic wind farm (8×6 array, dashed blue) from previous LES simulation by Verhulst [15]. (b) Spectral convergence of the eignevalue spectrum λ_m/λ_1 for finite sized wind farm. Snapshot separation, black – $4T_e/5$, red – $3T_e/5$, blue – $2T_e/5$ and magenta – $T_e/5$

In the next section, we discuss the Fourier-POD methodology for complex fourier-transformed velocity snapshots.

3.2. Fourier-POD methodology

For the Fourier-POD methods, analogous to the projections methods of 3D POD, we can write the projection $\mathbf{P}_{f,r}$ as

$$\mathbf{P}_{f,r}\boldsymbol{u}'_m = \int_{-\infty}^{\infty} \sum_{j=0}^{r-1} (\hat{\boldsymbol{\varphi}}_j, \hat{\boldsymbol{u}}'_m)\hat{\boldsymbol{\varphi}}_j e^{ik_y y} \mathrm{d}y = \int_{-\infty}^{\infty} \sum_{j=0}^{r-1} \hat{a}_j(k_y, t_m)\hat{\boldsymbol{\varphi}}_j(x, z, k_y) e^{ik_y y} \mathrm{d}y, \quad r \leq N_t \tag{7}$$

In a similar spirit, the correlation matrix can be written as

$$\hat{C}_{mn} = \frac{1}{N_t}(\hat{\boldsymbol{u}}'(x, k_y, z, t_m), (\hat{\boldsymbol{u}}'(x, k_y, z, t_n)) \tag{8}$$

where $\hat{\boldsymbol{u}}'$ is the Fourier transform in the lateral/spanwise y direction of the velocity fluctuation vector $\boldsymbol{u}'(\boldsymbol{x}, t_m)$.

$$\hat{\boldsymbol{u}}'(x, k_y, z, t_m) = \frac{1}{2\pi}\int_{-\infty}^{\infty} \boldsymbol{u}'(x, y, z, t_m)e^{-ik_y y}\mathrm{d}y \tag{9}$$

Since the snapshots in FPOD methods are complex valued rather than being real-valued as in the 3D POD case, the modes are expected to be complex in nature as well. Note, however that the correlation coefficient (3D POD as well as 2D Fourier-POD) are based on the inner products of snapshots. If χ is a matrix containing columns of snapshot $\chi_i = [\chi_1, \chi_2, \chi_3, \ldots, \chi_n]$, then the correlation matrix can be written as $\chi\chi^T$ while for complex snapshots (e.g., 2D FPOD), the inner product can be written as $\chi\chi^H$, where $[]^T$ and $[]^H$ represent transpose and Hermitian (complex conjugate transpose) respectively. Subsequently, it is apparent that while the eigenvectors and hence the modes can be complex for

Preprints (www.preprints.org) | NOT PEER-REVIEWED | Posted: 26 February 2020 doi:10.20944/preprints202002.0390.v1

Peer-reviewed version available at Energies 2020, 13, 1660; doi:10.3390/en13071660

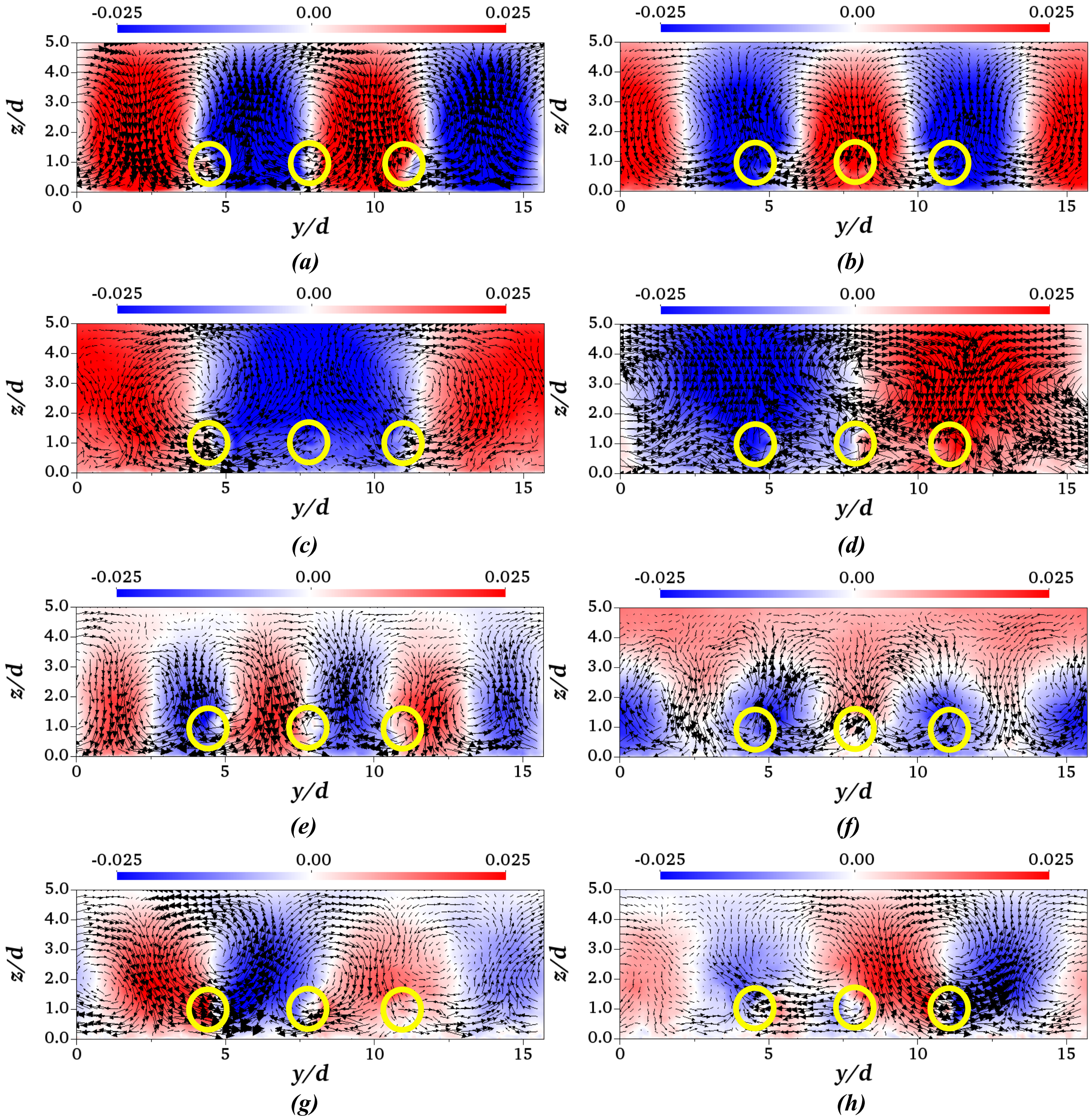

Figure 3. Normalized POD mode for (a) $k = 0$, (b) $k = 1$, (c) $k = 2$, (d) $k = 3$, (e) $k = 4$, (f) $k = 5$, (g) $k = 6$, (h) $k = 7$. Red-blue contours indicate the normalized streamwise velocity modes, $\varphi_k^u \sqrt{\lambda_k}/U_\infty$ overlayed with in-plane spanwise and vertical modes, $\varphi_k^v \sqrt{\lambda_k}/U_\infty$, $\varphi_k^w \sqrt{\lambda_k}/U_\infty$ as vectors. Yellow circles– turbine locations.

Preprints (www.preprints.org) | NOT PEER-REVIEWED | Posted: 26 February 2020 doi:10.20944/preprints202002.0390.v1
Peer-reviewed version available at Energies 2020, 13, 1660; doi:10.3390/en13071660

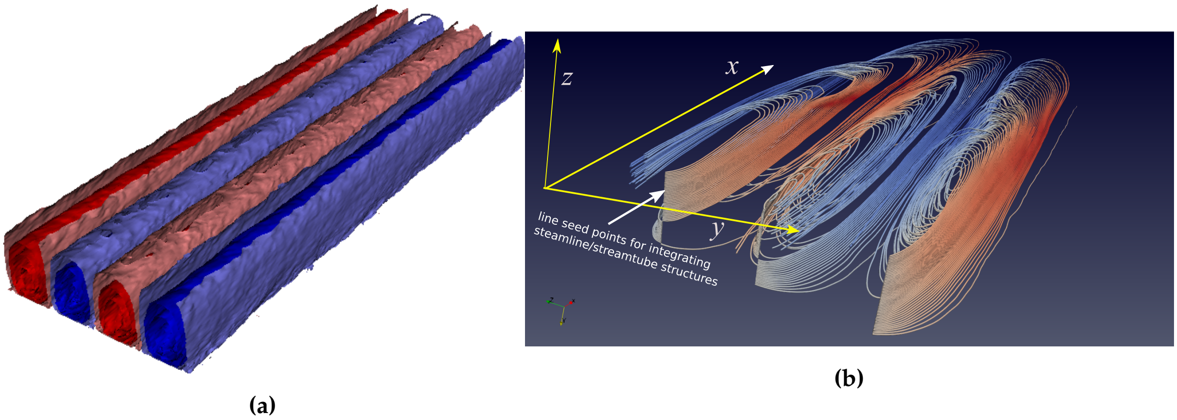

Figure 4. 3D normalized POD mode, $k = 0$ (a) Isosurface levels of streamwise POD mode for $\varphi_k^u \sqrt{\lambda_k}/U_\infty$ (b) Streamtubes of vector streamwise POD mode for $\varphi_k^{u,v,w} \sqrt{\lambda_k}/U_\infty$

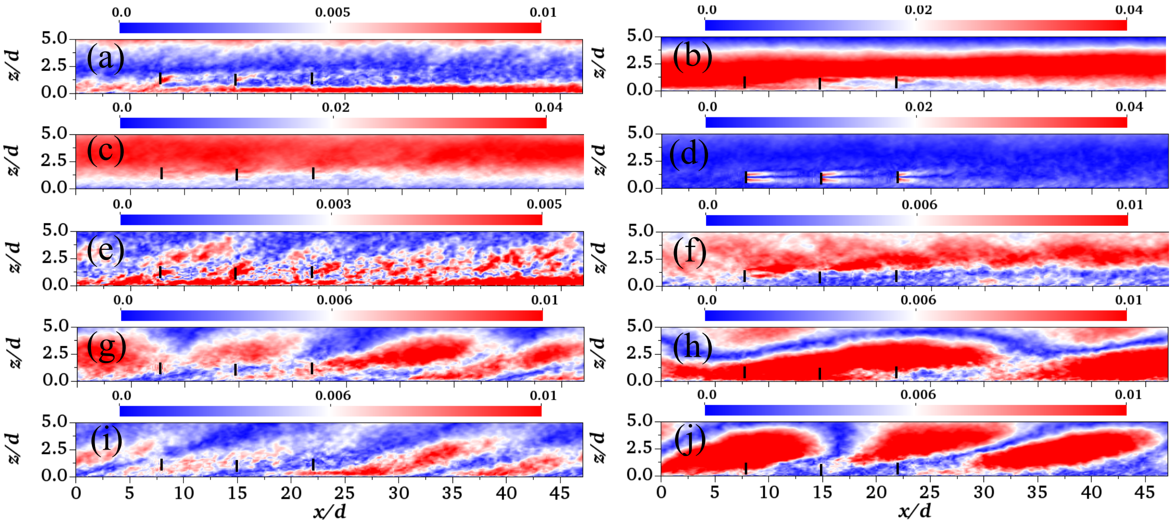

Figure 5. Normalized POD mode for (a) $k = 0$, (b) $k = 1$, (c) $k = 2$, (d) $k = 3$, (e) $k = 4$, (f) $k = 5$, (g) $k = 6$, (h) $k = 7$, (h) $k = 8$, (h) $k = 9$. Red-blue contours indicate the normalized velocity magnitude modes, $|\varphi_k^u \sqrt{\lambda_k}/U_\infty|$. Thick black vertical lines – turbine locations.

FPOD, the eigenvalues (or the diagonal eigenvalue matrix) are given by $diag(\lambda) = \Sigma\Sigma^H$ (since svd can be complex for real systems), where Σ is the matrix containing singular values at diagonal entries from the SVD of the snapshot matrix χ. Consequently, the eigenvalues of 3D POD as well as complex 2D Fourier-POD are always real-valued and represent kinetic energy comtent the mode. The FPOD analysis has been carried out in an open-source python code MODRED [57] written as a high-level class interface using spectral methods.

Before moving into the results related to Fourier-POD analysis, we present the spanwise Fourier energy spectra of the velocity snapshots (Figure 7).

The spanwise spectra (averaged in the streamwise, vertical direction as well as time) can be given as

$$\langle \tilde{E}_{u_i'} \rangle_{x,z,T_{avg}} = \frac{1}{T_{avg}} \int_0^{T_{avg}} \Big[\frac{1}{L_x L_z} \int_{x_{min}}^{x_{max}} \int_{z_{min}}^{z_{max}} u_i'(x, \lambda_y, z, t)^* u_i'(\chi, \lambda_y, z, t) \mathrm{d}y\mathrm{d}z \Big] \mathrm{d}t, \quad (10)$$

where x, y are the streamwise and spanwise direction respectively. Note the presence of the $\lambda^{11/3}$ or $k_y^{-11/3}$ law near the tail of the spectrum. This appears to be a filtering of the $k_y^{-5/3}$ spectrum, as $G(k_y)k_y^{-5/3}$, with $G(k_y) = k_y^{-2}$ spectrum. Such filtering is possibly an outcome of vertical averaging of the spectra, streamwise averaging of the heterogeneity owing to wind turbine array and is mainly an observational documentation. Note for performing the Fourier transform a total of 512 uniform

Preprints (www.preprints.org) | NOT PEER-REVIEWED | Posted: 26 February 2020 doi:10.20944/preprints202002.0390.v1

Peer-reviewed version available at Energies 2020, 13, 1660; doi:10.3390/en13071660

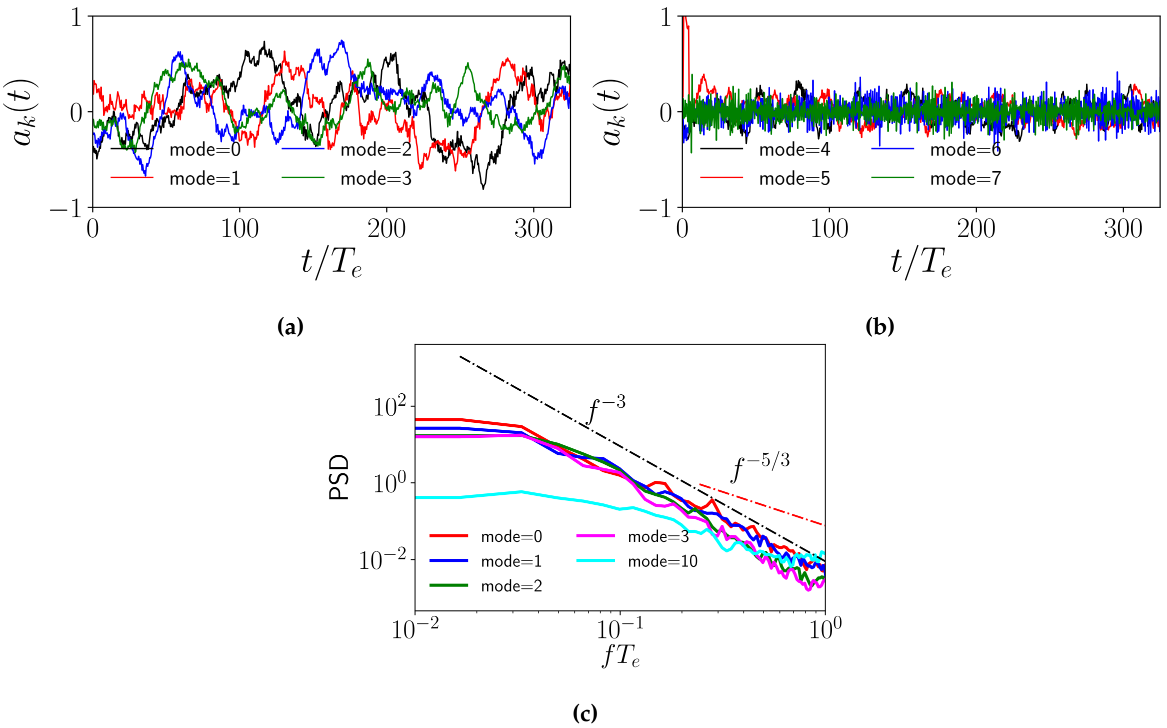

Figure 6. (a), (b) Projection coefficient of 3D POD modes, $a_k(t)$ vs time normalized by flow-through time, $T_e = 15\pi D/U_\infty$. (c) Power spectral density of the projection coefficients vs normalized frequency, fT_e.

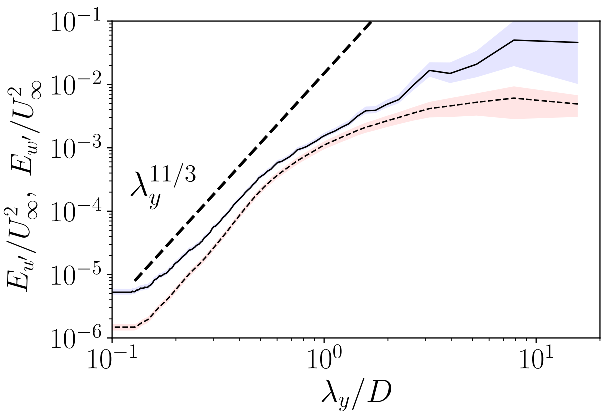

Figure 7. u (solid), w (dashed) energy spectra and their variability ($\pm$ twice the standard deviation; transparent blue and red). Energy spectra computed in spanwise wavenumber space, averaged temporally and in the streamwise, wall normal direction

grid points are chosen in the spanwise/lateral direction which ensures a total of lateral resolved length scale (Nyquist limit) of $5\pi d/256 = 0.06d$, which is lower than what the LES simulation with Navier-Stokes solver could resolve (1). Such a high number of grid points for the FFT ensure that the aliasing error could be avoided during the reconstruction of the 3D POD mode from the 2D complex Fourier-POD modes. Figure 7 not only indicates energy cascade from the larger to the smaller length scales in the spanwise spectra, but also illustrates that the larger length scales are associated with higher degrees of uncertainties (larger decorrelation time scales) than their smaller scale counterpart. Figure 8 manifesting the Fourier-transformed velocity magnitude serves as a sanity test of the Fourier-transform itself, with the snapshot at $k_y d = 0$ representing the temporal snapshot of spanwise averaged velocity magnitude, while the same for $k_y d = 2$, manifests wake-imprints from finer scale fluctuations.

Preprints (www.preprints.org) | NOT PEER-REVIEWED | Posted: 26 February 2020 doi:10.20944/preprints202002.0390.v1

Peer-reviewed version available at Energies 2020, 13, 1660; doi:10.3390/en13071660

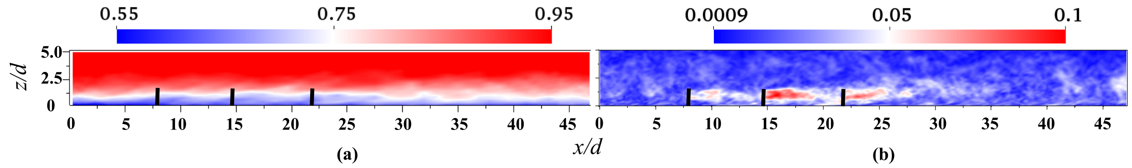

Figure 8. Snapshots of Fourier-transformed velocity magnitude, $||u||$ for spanwise wavenumbers, (a) $k_yd = 0$ and (b) $k_yd = 2.0$. Thick black vertical lines - turbine locations.

From equation 2 and 7, we can define the complex velocity magnitude mode from the POD analysis as $||\boldsymbol{u}|| = \sqrt{|\hat{u}|^2 + |\hat{v}|^2 + |\hat{w}|^2}$ and $|\hat{u}_i| = [\mathcal{R}(\hat{u}_i)^2 + \mathcal{I}(\hat{u}_i)^2]^{1/2}, \forall i = 1, 2, 3..$ Additionally, the phase of the complex POD mode can also be defined as $\psi_{u_i} = \arctan(\mathcal{I}(\hat{u}_i)/\mathcal{R}(\hat{u}_i))$

Figure 9a illustrates the eigenspectra of the 2D complex field snapshots (spanwise Fourier transformed velocity) documented at different wave numbers. Expectedly, we observe that the eigenspectra has slower decay with modes as we move to higher wavenumbers or smaller spanwise length scales (laterally thin structures). This is manifested by the spectra getting flatter for higher wavenumbers. This indicates that for turbulent structures which are laterally thin (higher k_y), the energy content does not vary significantly based on the POD ranks and should approach towards a uniform distribution of eigenspectra at $k_y \to \infty$ (isotropization of small scales). Figure 9b shows the convergence of the Fourier-POD modes for a representative wavenumber of $k_yd = 2$. While similar results can be obtained for other wavenumbers, it is striking to note that the FPOD eigenspectra converge much better than the 3D POD eigenspectra at all modes. Since the number of snapshots and the spacing between the snapshots are the same for the 3D POD and 2D Fourier-POD analysis, the only way this is possible is when most of the uncertainty manifested at the larger length scales are contained in the Fourier energy spectra as is evident in Figure 7. It is worth noting that the Fourier-modes are analytical descriptors of the POD modes with periodic boundary conditions [22]. Consequently, a FPOD type of decomposition for a wind farm with spanwise periodic boundary conditions, by construction, picks up the correct spanwise modes without running into convergence issues. The 3D POD modes are supposed to converge to the FPOD modes asymptotically with the increase in the number of snapshots.

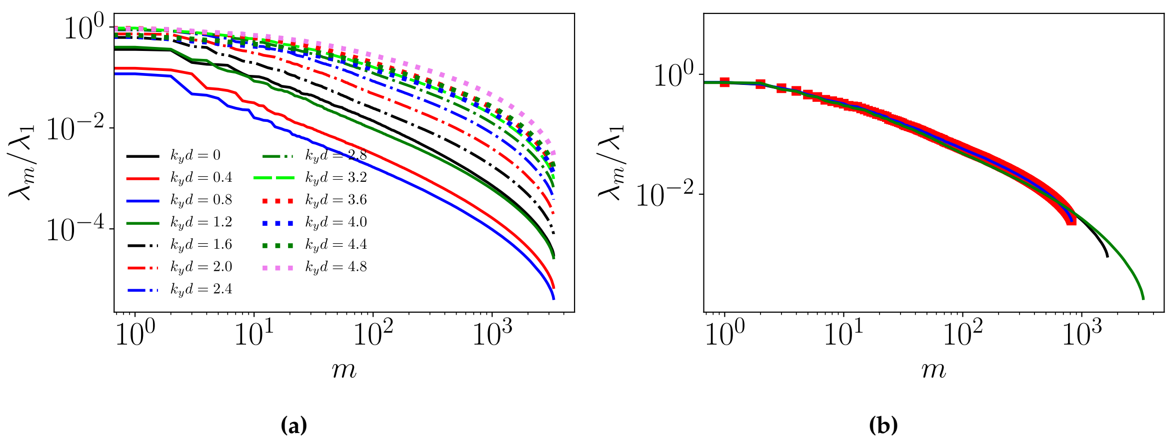

Figure 9. (a) Normalized eigenspectra λ_m/λ_1 for different wavenumbers k_y for the Fourier-POD modes. (b) Convergence of the normalized eigenspectra λ_m/λ_1 for wavenumber $k_yd = 2$. Different snapshot spacing, $T_e/5$ – green, $2T_e/5$ – black, $4T_e/5$ -blue, $4T_e/5$ (not considering the reflected data) – red square.

In Figures 10a, 10b, 10c, we illustrate the behaviour of the FPOD eigenspectra for lower and higher wavenumbers. What is striking, is that we can capture a m^{-1} scaling law for modes spanning a decade from $m = 10 - 100$ for wavenumbers $k_yd < 2.0$. For the number of snapshots considered, we observed a scaling law of $m^{-0.8}$ in the 3D POD eigenspectra. Interestingly, we also observe this scaling of FPOD

Preprints (www.preprints.org) | NOT PEER-REVIEWED | Posted: 26 February 2020 doi:10.20944/preprints202002.0390.v1

Peer-reviewed version available at Energies 2020, 13, 1660; doi:10.3390/en13071660

eigenspectra at 25% of the total number of snapshots ($\sim$ 1600 snapshots) used in eigen-decomposition, where we were only able to capture $m^{-0.5}$ scaling for the 3D POD eigenspectra [16]. This is one of our most crucial observations in the whole analysis. We observe that the scaling exponent gradually decay as we consider the eigenspectra at higher wavenumbers indicating a flatter spectral tail as was discussed above (more isotropization of structures). The results have two implications; i) The m^{-1} ($m^{-0.9}$ [15].) scaling is not an "artifact of the lack of convergence" and is observed in laterally wide turbulent structures for FPOD modes $m > 10$. Interestingly, similar scaling laws ($m^{-1.2}$) were also noted by Hamilton and coworkers [27] for 2D POD of wind turbine arrays at different streamwise locations. For FPOD eigenspectra, as the turbulent eddies become thinner, the scaling exponents become larger and tend closer to zero (for higher wavenumbers). Note, in 3D POD we were not able to capture scaling laws of m^{-1} or $m^{-0.9}$, owing to the lack of enough number of snapshots to cover several decorrelation times of the larger scales of interest (higher uncertainties in the larger coherent scales). In the FPOD analysis, we were not only able to decouple the length scales in the spanwise (Fourier) and streamwise(POD) direction, but were also able to decouple the uncertainties – with the Fourier energy spectra carrying most of the uncertainty. Consequently we were able to capture the scaling laws of the FPOD modes (less uncertainty due to better convergence) accurately.This analysis shows that while FPOD expectedly cannot essentially improve the POD results, they have the potential to provide crucial insights to the lack of convergence in the 3D POD eigenspectra and hence their scaling laws.

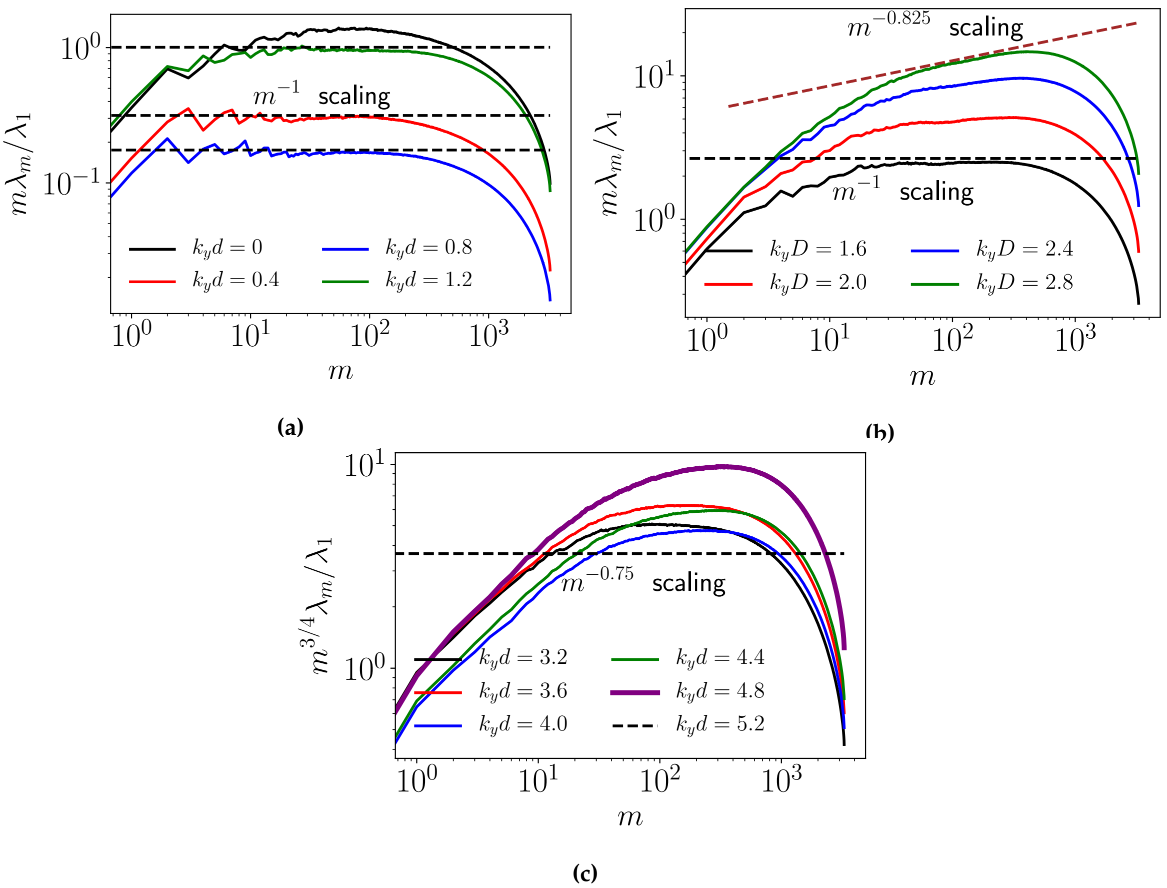

Figure 10. Premultiplied normalized eigenspectra for different wavenumbers k_y for the Fourier-POD modes. (a) $m\lambda_m/\lambda_1$, for $k_yd = 0, 0.4, 0.8, 1.2$. (b) $m\lambda_m/\lambda_1$, for $k_yd = 1.6, 2, 2.4, 2.8$ (c) $m^{3/4}\lambda_m/\lambda_1$, for $k_yd = 3.2, 3.6, 4.0, 4.4, 4.8, 5.2$.

In Figures 11- 14, we illustrate the Fourier-POD eigenmodes for wavenumbers $k_yd = 0, 0.4, 0.8, 1.2$. Interestingly, for all modes $m = 0$, $\forall k_y$, we see homogeneous/quasi-homogeneous streaks in the

Preprints (www.preprints.org) | NOT PEER-REVIEWED | Posted: 26 February 2020 doi:10.20944/preprints202002.0390.v1

Peer-reviewed version available at Energies 2020, 13, 1660; doi:10.3390/en13071660

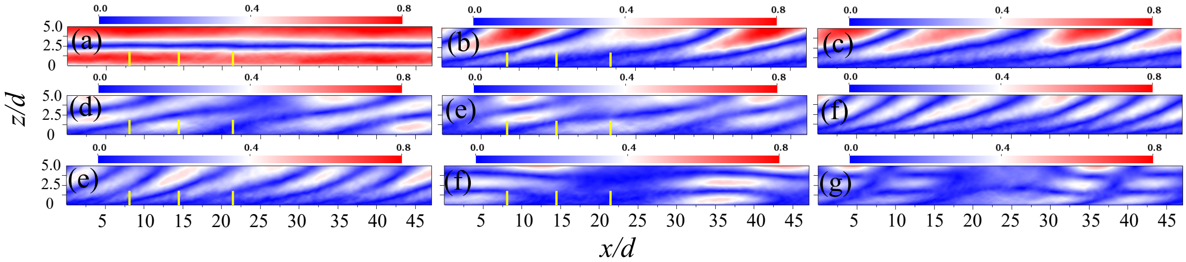

Figure 11. Normalized Fourier-POD mode for wave-number (POD of spanwise averaged snapshot data), $k_y d = 0$. (a) $m = 0$, (b) $m = 1$, (c) $m = 2$, (d) $m = 3$, (e) $m = 4$, (f) $m = 5$, (g) $m = 6$, (h) $m = 7$, (h) $m = 8$. Red-blue contours indicate the normalized velocity magnitude modes, $|\varphi_k^{\boldsymbol{u}} \sqrt{\lambda_k}/U_\infty|$. Thick yellow vertical lines – turbine locations.

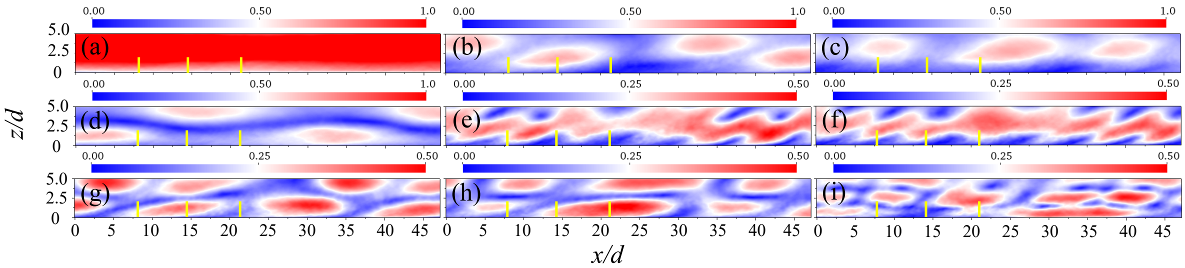

Figure 12. Normalized Fourier-POD mode for wave-number, $k_y d = 0.4$. (a) $m = 0$, (b) $m = 1$, (c) $m = 2$, (d) $m = 3$, (e) $m = 4$, (f) $m = 5$, (g) $m = 6$, (h) $m = 7$, (h) $m = 8$. Red-blue contours indicate the normalized velocity magnitude modes, $|\varphi_k^{\boldsymbol{u}} \sqrt{\lambda_k}/U_\infty|$. Thick yellow vertical lines – turbine locations.

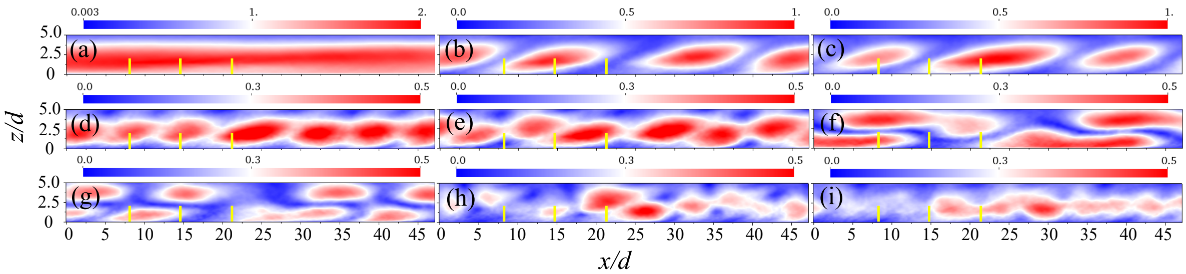

Figure 13. Normalized Fourier-POD mode for wave-number, $k_y d = 0.8$. (a) $m = 0$, (b) $m = 1$, (c) $m = 2$, (d) $m = 3$, (e) $m = 4$, (f) $m = 5$, (g) $m = 6$, (h) $m = 7$, (h) $m = 8$. Red-blue contours indicate the normalized velocity magnitude modes, $|\varphi_k^{\boldsymbol{u}} \sqrt{\lambda_k}/U_\infty|$. Thick yellow vertical lines – turbine locations.

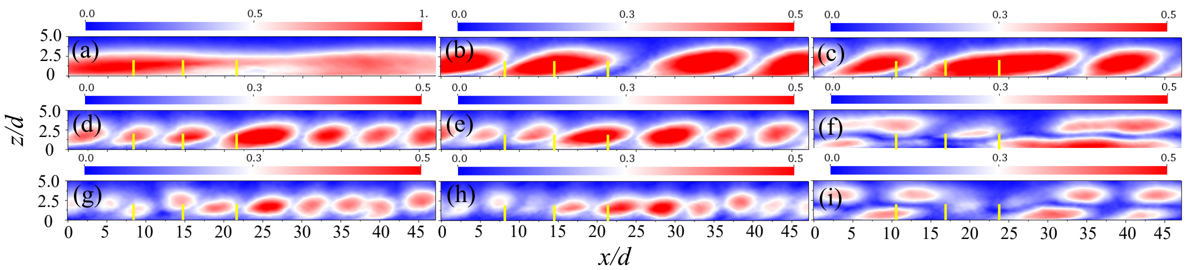

Figure 14. Normalized Fourier-POD mode for wave-number, $k_y d = 1.2$. (a) $m = 0$, (b) $m = 1$, (c) $m = 2$, (d) $m = 3$, (e) $m = 4$, (f) $m = 5$, (g) $m = 6$, (h) $m = 7$, (h) $m = 8$. Red-blue contours indicate the normalized velocity magnitude modes, $|\varphi_k^{\boldsymbol{u}} \sqrt{\lambda_k}/U_\infty|$. Thick yellow vertical lines – turbine locations.

Preprints (www.preprints.org) | NOT PEER-REVIEWED | Posted: 26 February 2020 doi:10.20944/preprints202002.0390.v1

Peer-reviewed version available at Energies 2020, 13, 1660; doi:10.3390/en13071660

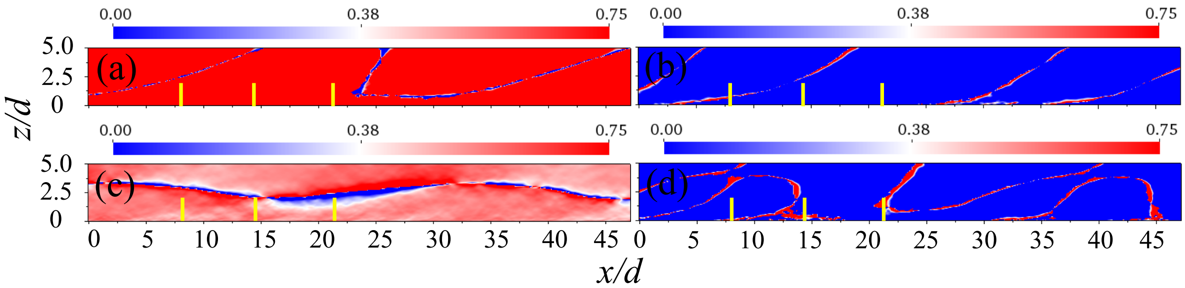

Figure 15. Phase of streamwise Fourier-POD mode for wave-number $k_y d = 0.4$. (a) $m = 1$, (b) $m = 2$, (c) $m = 3$, (d) $m = 4$. Red-blue contours indicate the phase of the streamwise modes, $\psi = \tan(\mathcal{I}(\varphi_k^u)\mathcal{R}(\varphi_k^u))$. Thick yellow vertical lines – turbine locations.

streamwise direction which are evidently the footprints of the "roll-cells" modulated by wake turbulence. Apart from the "roll cells", modes $m > 0$, $\forall k_y \geq 0.8$ also display large scale inclined structures ($k_y d = 0.8$, $m = 2-5$, $k_y = 1.2$, $m = 2-5$) which are essentially manifestations of "attached eddies" [6,53]. The FPOD's manifest that the attached eddies form at some threshold spanwise wavenumbers which could not be identified in 3D POD modes. These structures also display similarity to the modes computed from the 3D POD eigen decomposition. Additional to the "roll-cells" and "attached eddy" foot-prints, we observe another type of mode, which are reminiscent of wave like features ($k_y d = 0.4$, $m \gtrapprox 4$, $k_y d = 0.8-1.2, m = 6$). The feature is most conspicuous for $k_y = 0.4, m = 4$. Such modes might be manifestation of wave modulation of large turbulent structures at the particular wavenumber $k_y = 4$, but further studies are needed to speculate the hypothesis. Interestingly, we also observe that as $k_y d$ increases (laterally thin structures) the streamwise size of the inclined structures/attached eddies remain approximately the same for a fixed mode number and the streamwise length scale progressively decreases with increasing mode size. This manifests disintegration/cascading of larger eddies to their smaller counterpart.

Figure 15 illustrate the phase of the complex streamwise FPOD modes for mode $m \leq 4$. The streamwise FPOD modes are dominant compared to their lateral and vertical counterparts. It is interesting to observe that the mode phase ψ changes sign at the edge/boundaries of the large scale eddies and hence is expectedly a great method to visualize the edges of the turbulent structures.

3.3. Reconstruction of 3D modes from Fourier-POD

In this final section we deal with the reconstruction of the three-dimensional modes obtained by performing inverse fourier transform of the complex Fourier-POD 2D modes. The three dimensional reconstruction of the modes, $\widetilde{\boldsymbol{\varphi}}_j(x,y,z)$ can be obtained as

$$\widetilde{\boldsymbol{\varphi}}_j(x,y,z) = \frac{1}{2\pi}\int_{-k_{max}}^{k_{max}} \hat{\boldsymbol{\varphi}}_j(x,k_y,z)e^{ik_y y}\mathrm{d}y \tag{11}$$

. Note mathematically, $\widetilde{\boldsymbol{\varphi}} \neq \boldsymbol{\varphi}$ (3D POD) as will be established later from the structure of the correlation matrix.

The correlation matrix for FPOD can be written as

$$\begin{aligned} C_{mn} &= (\boldsymbol{u}(x,k_y,z,t_m), \boldsymbol{u}(x,k_y,z,t_n)) \\ &= \int_\Omega \boldsymbol{u}(x,k_y,z,t_m)\boldsymbol{u}^*(x,k_y,z,t_n)\mathrm{d}V \\ &= (\int_{-k_{max}}^{k_{max}} \hat{\boldsymbol{u}}_j(x,k_y,z,t_m)e^{iky}\mathrm{d}k, \int_{-k_{max}}^{k_{max}} \hat{\boldsymbol{u}}_j^*(x,k_y,z,t_n)e^{-ik'y}\mathrm{d}k') \end{aligned} \tag{12}$$

Preprints (www.preprints.org) | NOT PEER-REVIEWED | Posted: 26 February 2020 doi:10.20944/preprints202002.0390.v1
Peer-reviewed version available at Energies 2020, 13, 1660; doi:10.3390/en13071660

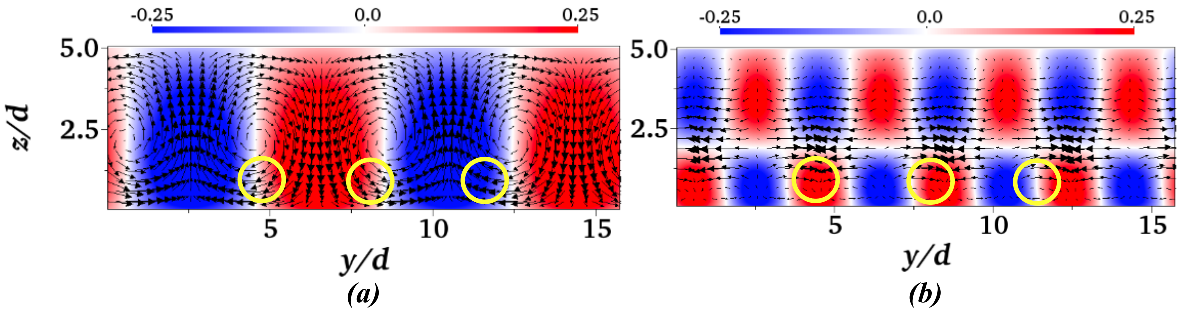

Figure 16. Reconstructed 3D POD modes from 2D Fourier-POD modes at yz plane - $x = 7.85d$, (a) $m = 0$, inverse FFT $\forall k_y d = 0.8$, (b) $m = 1$, inverse FFT, $\forall k_y d = 0.8$. Contours - $\tilde{\phi}^u$, in-plane vectors - $\tilde{\phi}^v, \tilde{\phi}^w$ Thick yellow circles – turbine locations.

Note for the inner-product in the physical space ($\int_\Omega()()^* \mathrm{d}V$), the complex conjugate (denoted by *) of the real velocity snapshot is the velocity snapshot itself. For brevity of analysis, we use the symbol k instead of k_y for spanwise wavenumbers in subsequent derivations.

$$\begin{aligned} C_{mn} &= (\iint_{-k_{max}}^{k_{max}} \int_\Omega \hat{\boldsymbol{u}}_j(x,k_y,z,t_m)\hat{\boldsymbol{u}}^*{}_j(x,k_y,z,t_n)e^{i(k-k')y}\mathrm{d}k\mathrm{d}k'\mathrm{d}V) \\ &= \left(\iint_{-k_{max}}^{k_{max}} [\int_\Omega \hat{\boldsymbol{u}}_j(x,k_y,z,t_m)\hat{\boldsymbol{u}}^*{}_j(x,k_y,z,t_n)e^{i(k-k')y}\mathrm{d}V]\mathrm{d}k\mathrm{d}k'\right) \end{aligned} \tag{13}$$

Since $\displaystyle\int_\Omega \mathrm{d}V = \int_0^{L_x}\int_0^{L_y}\int_0^{L_z} \mathrm{d}x\mathrm{d}y\mathrm{d}z$ and $\int_\Omega \hat{\boldsymbol{u}}^*{}_j(x,k',z,t_m)\hat{\boldsymbol{u}}_j(x,k,z,t_n)\mathrm{d}x\mathrm{d}y = \hat{\hat{C}}_{mn}(k,k')$, we have a relation between C_{mn} and $\hat{C}_{mn}$ as follows.

$$C_{mn} = \int_0^{L_y}\iint_{-k_{max}}^{k_{max}} \hat{\hat{C}}_{mn}(k,k')e^{i(k-k')y}\mathrm{d}k\mathrm{d}k'\mathrm{d}y \tag{14}$$

Realizing $\hat{C}_{mn}(k) = \hat{\hat{C}}_{mn}(k, k' = k)$, with the assumption that the temporal correlation of the snapshots are the strongest when the wavenumbers $k = k'$. Equation 14 can be simplified as

$$C_{mn}(k) \approx \iint_{-k_{max}}^{k_{max}} \hat{C}_{mn}(k)\left(e^{i\Delta k L_y} - 1)/i\Delta k\right)\mathrm{d}k\mathrm{d}k' \tag{15}$$

Note, the integration does not have a closed form. However, the function in the integrand $\left(e^{i\Delta k L_y} - 1)/i\Delta k\right)$ is bounded between 0 ($k_{max} \longrightarrow \infty$ and finite complex constant $L_y[1+i]$. Thus, we can comment that $\hat{C}_{mn}(k)$ is bounded if C_{mn} is bounded as well. Additionally, since the (x,z) spatial structure of C_{mn} and $\hat{C}_{mn}$ are the same (from Equation 13), the eigenvalue scaling laws for the FPOD modes are similar to its 3D counterpart indicating that the scaling laws are a manifestation of the streamwise dominance of the large scale eddies.

We present the reconstruction of the 3D POD modes by inverse Fourier transform (IFFT) of the FPOD modes as illustrated in Equation 11. Figure 16 represents the reconstructed mode by IFFT of FPOD modes, $m = 0$, $m = 1$ for $k_y d = 0.8$ ($k_y = 2$). Figure 17 illustrates similar such reconstruction, but for $k_y = 1.6$ ($k_y = 4$). Finally, Figure 18 illustrates the reconstructed modes by performing IFFT of $m = 1$, for a set of wavenumbers $k_y d = 0 - 1.2$ ($k_y = 0 - 4$) and $k_y d = 0 - 1.6$ ($k_y = 0 - 5$). From a more quantitative perspective, the reconstructed 3D POD modes from the FPOD that are illustrated in this paper, can be given as

$$\tilde{\boldsymbol{\varphi}}_j(x,y,z) = \frac{1}{2\pi}\int_{-k_{max}}^{k_{max}} \hat{\boldsymbol{\varphi}}_j(x,k_y,z)W(k_y)e^{ik_y y}\mathrm{d}k_y \tag{16}$$

Peer-reviewed version available at Energies 2020, 13, 1660; doi:10.3390/en13071660

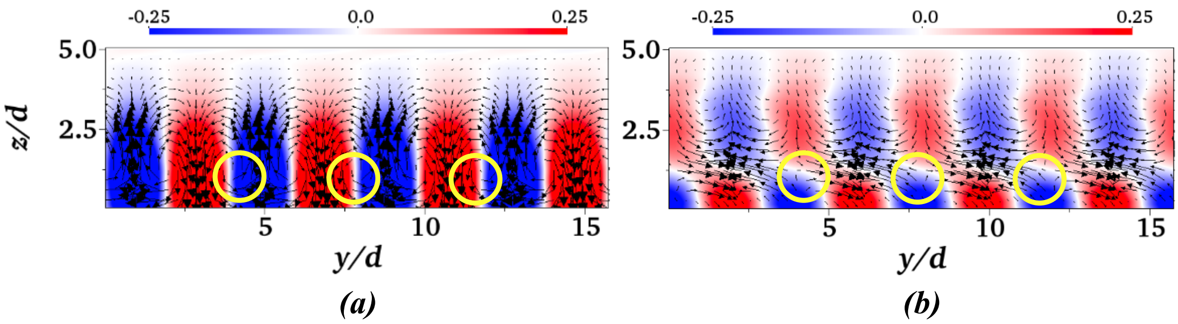

Figure 17. Reconstructed 3D POD modes from 2D Fourier-POD modes at yz plane - $x = 7.85d$, (a) $m = 0$, inverse FFT $\forall k_y d = 1.6$, (b) $m = 1$, inverse FFT, $\forall k_y d = 1.6$. Contours - $\tilde{\phi}^u$, in-plane vectors - $\tilde{\phi}^v, \tilde{\phi}^w$. Thick yellow circles – turbine locations.

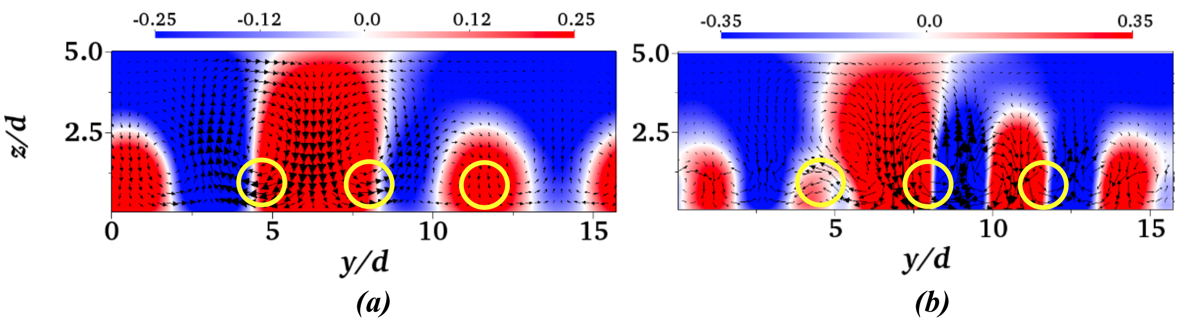

Figure 18. Reconstructed 3D POD modes from 2D Fourier-POD modes at yz plane - $x = 7.85d$, (a) $m = 0$, inverse FFT $\forall k_y d = 0 - 1.2$, (b) $m = 0$, inverse FFT, $\forall k_y d = 0 - 1.6$. Contours - $\tilde{\phi}^u$, in-plane vectors - $\tilde{\phi}^v, \tilde{\phi}^w$. Thick yellow circles – turbine locations.

Here, $W(k_y)$ is a weight function of wavenumbers which act as a filter to the Fourier transform. For Figures 16 and 17, $W(k_y) = 1$ for $k_y = \pm 2$ and $k_y = \pm 4$, respectively, while $W(k_y) = 0$ for all other wavenumbers. For Figure 18, $W(k_y) = 1 \forall - B \leq k_y \leq B$ ($B = 3$, for Figure 18 (a), $B = 4$, for Figure 18 (b)) and $W(k_y) = 0$ for all other wavenumbers. In other words, while Figures 16, 17 illustrate single spanwise modes, Figure 18 represents summation of the first several most dominant spanwise modes for a particular m. The reconstruction methodology is motivated by the fact that the first two dominant modes (highest contributors of kinetic energy) have two-pairs of counter-rotating roll-cells or four vortical structures corresponding to an "apparent wavenumber" of 2 [15]. The partial reconstructions (via IFFT), shown in Figure 18, further illustrate the importance of the $3-4$ pairs ($k_y = 3, 4$) of counter-rotating roll-cells in the dominant mode shapes contributing to the reconstruction, despite having a dominant Fourier mode $k_y = 2$ identified as the most energetic POD mode. Note, also that the partial reconstructions give rise to variable size and shape of the modes as opposed to reconstructions by IFFT involving a single wave number or modes obtained from the 3D POD decomposition. This can be probably attributed to the exponential premultiplier term $\left(e^{i\Delta k L_y} - 1\right)/i\Delta k\right)$ referred in Equation 15 that alter the y variation of the FPOD correlation matrix as opposed to the 3D-POD correlation matrix. While examining the $m = 0$ and $m = 1$ mode composition for $k_y\, d = 0.8$ and $k_y\, d = 1.6$ that correspond to the most dominant 3D POD modes (Figures 16, 17), an interesting fact can be observed. It can be seen that the modes $m = 0$ illustrate the global mechanisms of momentum transfer via ejections and sweeps (updrafts and downdrafts) across the entire boundary layer depth, i.e. the global interactions between the inner and outer layer, as 3D POD modes capture as well. However, $m = 1$ modes illustrate a "bi-layer" structure, corresponding to a momentum transfer between the wind turbine wake region and the inner/outer layer respectively. These modes, which characterize the important energetic mechanisms in wind-farm/ABL interactions, are not picked up by the 3D POD decomposition, while they are by FPOD. The analysis involving the 3D-POD, 2D Fourier-POD and the reconstruction of

Preprints (www.preprints.org) | NOT PEER-REVIEWED | Posted: 26 February 2020 doi:10.20944/preprints202002.0390.v1

Peer-reviewed version available at *Energies* **2020**, *13*, 1660; doi:10.3390/en13071660

the 3D modes from FPOD reveals that, while one-to-one mapping of the 3D POD modes and the reconstructed 3D modes by the mode ranks, m, is difficult at this stage, it shows the importance of counter-rotating roll-cell structures involving ejections and sweeps in wind farms and the atmospheric boundary layers in general.

4. Conclusions

In the current manuscript we have analysed the dynamics of large turbulent structures in a heterogeneous finite-sized wind canopy using three-dimensional proper orthogonal decomposition. Large counter-rotating roll-cell structures as well as inclined wall-attached structures have been identified in this analysis. The current analysis further reveals that substantial number of snapshots are required to obtain the convergence of the scaling trends of the POD eigenspectra, or in particular, the $m^{-0.9}$ law. In a heterogeneous wind-farm, where artificial snapshots cannot be created exploiting the domain homogeneity (shifting in periodic wind farms) [15], the eigenspectra does not converge well beyond mode $m > 10$. The lack of convergence is attributed to the uncertainty (higher decorrelation times) in the large scale structures which are still present even in high-order POD modes m>10 (cf., e.g., Figure 3). Consequently, the scaling trend is slightly deviated to $m^{-0.8}$. This led us to adapt a novel Fourier-POD methodology (FPOD), to gain further insights on the convergence of eigenspectra as well as the dynamics of large scale modes. FPOD essentially performs the POD eigendecomposition of the laterally Fourier-tranformed two dimensional complex velocity snapshots at each wavenumber as opposed to the three dimensional physical velocity for the 3D POD. The Fourier-POD analysis helps us gain valuable insights on the convergence of the eigenspectra by decoupling the length scales in the spanwise and streamwise direction. In particular it shows that the laterally wider structures are responsible for the $m^{-0.9}/m^{-1}$ scaling laws, while the spanwise thinner structures manifest $m^{-\beta}$ where $\beta < 0.9$. Additionally, we show excellent convergence of the Fourier-POD eigenspectra, indicating that the uncertainty of the larger turbulent scales are mostly contained in the Fourier energy spectra, rather than the FPOD modes. Finally, we look into the reconstruction of the 3D modal structures by performing inverse FFT operations on the 2D FPOD modes. From the mathematical analysis of the functional form of the correlation matrix, we provide deep insights about the similarities in the eigenspectra scaling and the modal shapes of the FPOD and 3D-POD. Eventually, our study reconstructs 3D POD modes from the 2D FPOD modes, which further provides guidance towards the understanding of the modal structure in wind farms. From the fundamental perspective, we have seen that the roll-cells are phenomenologically rudimentary structures contributing to the global sweeps and ejections. While [15] have predicted the contribution of such structures towards the kinetic energy entertainment in infinite wind farms, our studies corroborate such structures to be rather a fundamental property of rough ABL flows and are modulated by the wind turbines at rotor scales. Finally, even though our study was performed in the context of a finite-sized wind turbine array, it introduces a novel framework of Fourier-POD modal analysis, which can be useful for analysis of turbulent flows in other flow domains and configurations, as long as they possess one periodic direction.

Author Contributions: Conceptualization, T.C. and Y.P.; methodology,validation,investigation, visualization T.C.; writing–original draft preparation, T.C.; writing–review and editing, Y.P.; funding acquisition, Y.P.

Funding: The authors T. Chatterjee and Y. T. Peet would like to acknowledge the support of NSF-CBET 1335868 grant and the compute hours from XSEDE research allocations TG-ENG140005, TG-ENG150019 for their present work.

Acknowledgments: The 3D POD analysis has been carried out using open-source spectral element code Nek5000, while the Fourier-POD methodology has been carried out using open-source parallel python code MODRED. The authors would also like to thank Dr. Philip Sakievich, Sandia National Laboratories, for providing efficient VTK wrapper and routines for efficient handling of data structures in MODRED.

Conflicts of Interest: The authors declare no conflict of interest.

1. Fang, J.; Porté-Agel, F. Large-eddy simulation of very-large-scale motions in the neutrally stratified atmospheric boundary layer. *Boundary Layer. Meteorol.* **2015**, *155*, 397–416.
2. Calaf, M.; Meneveau, C.; Meyers, J. Large Eddy Simulation Study of Fully Developed Wind-Turbine Array Boundary Layers. *Phys. Fluids* **2010**, *22*, 015110.
3. Chamorro, L.P.; Lee, S.J.; Olsen, D.; Miliren, C.; Marr, J.; Arndt, R.; Sotiropoulos, F. Turbulence effects on a full-scale 2.5MW horizontal-axis wind turbine under neutrally stratified conditions. *Wind Energy* **2015**, *18*, 339–349.
4. Önder, A.; Meyers, J. On the interaction of very-large-scale motions in a neutral atmospheric boundary layer with a row of wind turbines. *J. Fluid. Mech.* **2018**, *841*, 1040–1072.
5. Chatterjee, T.; Peet, Y.T. Contribution of Large Scale Coherence to wind turbine power: A large eddy simulation study in periodic wind farms. *Physical Review Fluids* **2018**, *3*, 034601.
6. Balakumar, B.J.; Adrian, R.J. Large and very-large-scale motions in channel and boundary-layer flows. *Phil. Trans. R. Soc.* **2007**, *365*, 665–681.
7. Chamorro, L.P.; Porté-Agel, F. Turbulent Flow Inside and Above a Wind Farm: A Wind-Tunnel Study. *Energies* **2011**, *4*, 1916–1936.
8. Chauhan, K.; Hutchins, N.; Monty, J.; Marusic, I. Structure inclination angles in convective atmospheric surface layer. *Boundary Layer. Meteorol.* **2013**, *147*, 41–50.
9. Hutchins, N.; Chauhan, K.; Monty, J.; Klewicki, J. Towards reconciling the large-scale structure of turbulent boundary layers in the atmosphere and the laboratory. *Boundary Layer. Meteorol.* **2012**, *145*, 273–306.
10. Etling, D.; Brown, R. Roll vortices in planetary boundary layer: A review. *Boundary Layer. Meteorol.* **1993**, *65*, 215–248.
11. Young, G.S.; Kristovich, D.A.R.; Hjelmfelt, M.R.; Foster, R.C. Rolls, Streets, waves and more: A review of quasi-two-dimensional structures in the atmospheric boundary layer. *Bull. Am. Meteorol. Soc.* **2002**, *83*, 997–1001.
12. Kelley, N.D.; Jonkman, B.J.; Scott, G.N.; Bialasiewicz, J.T.; Redmond, L.S. The Impact of Coherent Turbulence on Wind Turbine AeroElastic Response and its simulation. WindPower 2017-1165, 2005. NREL/CP-500-38074.
13. Chamorro, L.; Hong, J.; Gangodagamage, C. On the scale-to-scale coupling between a full- scale wind turbine and turbulence. *J. Turbul.* **2015**, *16*, 617–632.
14. Cortina, G.; Sharma, V.; Calaf, M. Wind farm density and harvested power in very large wind farms: A low order model. *Physical Review Fluids* **2017**, *2*, 074601. doi:DOI: 10.1103/PhysRevFluids.2.074601.
15. VerHulst, C.; Meneveau, C. Large eddy simulation study of the kinetic energy entrainment by energetic turbulent flow structures in large wind farms. *Phys. Fluids* **2014**, *8*, 025113.
16. Peet, Y.T.; Chatterjee, T. The contribution of large scale structures in the power generation of finite scale wind farms using large eddy simulation. 2017. Proc. 10th International Symposium on Turbulence and Shear Flow Phenomena (TSFP10), Chicago, USA, July, 2017.
17. Zhang, M.; Stevens, R.J.A.M. Characterizing the Coherent Structures Within and Above Large Wind Farms. *Boundary-Layer Meteorology* **2019**. doi:10.1007/s10546-019-00468-x.
18. Stevens, R.J.; Gayme, D.F.; Meneveau, C. Effects of turbine spacing on the power output of extended wind-farms. *Wind Energy* **2016**, *19*.
19. Orell, A.; Preziuso, D.; Foster, N.; Morris, S.; Homer, J. 2018 Distributed Wind Market Report. Pacific Northwest National Laboratory operated by Battele, 2018. Online; U.S. Department of Energy, Office of Energy Efficiency and Renewable Energy (EERE).
20. Sirovich, L. Turbulence and dynamics of coherent structures. Part I: Coherent structures. *Q. J. Appl. Math.* **1987**, *XLV*, 561–571.
21. Park, H.; Sirovich, L. Turbulent thermal convection in a finite domain: Part II. Numerical results. *Physics of Fluids A: Fluid Dynamics* **1990**, *2*, 1659–1668, [https://doi.org/10.1063/1.857573]. doi:10.1063/1.857573.
22. Berkooz, G.; Holmes, P.; Lumley, J.L. The Proper Orthogonal Decomposition in the Analysis of Turbulent Flows. *Annual Review of Fluid Mechanics* **1993**, *25*, 539–575.

23. Bastankhah, M.; Porté-Agel, F. Wind tunnel study of the wind turbine interaction with a boundary-layer flow: Upwind region, turbine performance, and wake region. *Physics of Fluids* **2017**, *29*, 065105. doi:10.1063/1.4984078.
24. Towne, A.; Schmidt, O.T.; Colonius, T. Spectral proper orthogonal decomposition and its relationship to dynamic mode decomposition and resolvent analysis. *Journal of Fluid Mechanics* **2018**, *847*, 821–867. doi:10.1017/jfm.2018.283.
25. SCHMID, P.J. Dynamic mode decomposition of numerical and experimental data. *Journal of Fluid Mechanics* **2010**, *656*, 5–28. doi:10.1017/S0022112010001217.
26. Hamilton, N.; Tutkun, M.; Cal, R.B. Low-order representations of the canonical wind turbine array boundary layer via double proper orthogonal decomposition. *Physics of Fluids* **2016**, *28*.
27. Hamilton, N.; Tutkun, M.; Cal, R.B. Wind turbine boundary layer arrays for Cartesian and staggered configurations: Part II, low-dimensional representations via the proper orthogonal decomposition. *Wind Energy* **2015**, *18*, 297–315. doi:10.1002/we.1719.
28. GLEGG, S.; DEVENPORT, W. PROPER ORTHOGONAL DECOMPOSITION OF TURBULENT FLOWS FOR AEROACOUSTIC AND HYDROACOUSTIC APPLICATIONS. *Journal of Sound and Vibration* **2001**, *239*, 767 – 784. doi:https://doi.org/10.1006/jsvi.2000.3128.
29. Sakievich, P. Identification, Decomposition and Analysis of Dynamic Large-Scale Structures in Turbulent Rayleigh-Bénard Convection. PhD thesis, Arizona State University, 2017.
30. Pandey, S.; Schumacher, J. Reservoir computing model of two-dimensional turbulent convection, 2020, [arXiv:physics.flu-dyn/2001.10280].
31. Chatterjee, T.; Peet, Y. Large Eddy Simulation of a 3×3 wind turbine array using Actuator Line model with spectral elements. AIAA paper 2016–1988, 2016. 4 - 8 January 2016, San Diego, California.
32. Chatterjee, T.; Cherukuru, N.W.; Peet, Y.; Calhoun, R.J. Incorporating realistic geophysical effects of mean wind from LIDAR measurements in Large Eddy Simulation of Wind Turbine Arrays. *Journal of Physics: Conference Series* **2018**, *1037*, 072056. doi:10.1088/1742-6596/1037/7/072056.
33. Fischer, P.F.; Lottes, J.W.; Kerkemeier, S.G. Nek5000: an open source CFD solver, 2008. http://nek5000.mcs.anl.gov.
34. Deville, M.O.; Fischer, P.F.; Mund, E.H. *High-Order Methods for Incompressible Fluid Flow*; Cambridge University Press, Cambridge, UK, 2002.
35. Chatterjee, T.; Peet, Y. Incorporating realistic geophysical effects of mean wind from LIDAR measurements in Large Eddy Simulation of Wind Turbine Arrays. AIAA paper 2017-1165, 2017. 9-13 January, Grapevine, Texas.
36. McTavish, S.; Rodrigue, S.; Feszty, D.; Nitzsche, F. An investigation of in-field blockage effects in closely spaced lateral wind farm configurations. *Wind Energy* **2015**, *18*, 1989–2011, [https://onlinelibrary.wiley.com/doi/pdf/10.1002/we.1806]. doi:10.1002/we.1806.
37. Mason, P.J.; Thompson, D.J. Stochastic backscatter in large-eddy simulations of boundary layers. *J. Fluid. Mech.* **1992**, *242*, 51–78.
38. Porté-Agel, F.; Meneveau, C.; Parlange, M.B. A scale-dependent dynamics model for large eddy simulation: application to a neutral atmospheric boundary layer. *J. Fluid. Mech.* **2000**, *415*, 261–284.
39. Bou-Zeid, E.; Meneveau, C.; Parlange, M. A scale-dependent Lagrangian dynamic model for large eddy simulation of complex turbulent flows. *Phys. Fluids* **2005**, *415*, 025125.
40. Chatterjee, T.; Peet, Y.T. Effect of artificial length scales in large eddy simulation of a neutral atmospheric boundary layer flow: A simple solution to log-layer mismatch. *Physics of Fluids* **2017**, *29*, 075175. doi:10.1063/1.4994603.
41. Troldborg, N. Actuator Line Modeling of Wind Turbine Wakes. PhD thesis, Technical University of Denmark, 2008.
42. Chatterjee, T.; Peet, Y. Actuator Line Wind Turbine Simulations in Atmospheric Turbulent Flows using Spectral Element Method. AIAA paper 2015–0727, 2015. 5 - 9 January 2015, Kissimmmee, Florida.
43. Chatterjee, T.; Peet, Y.T. Exploring the benefits of vertically staggered wind farms: Understanding the power generation mechanisms of turbines operating at different scales. *Wind Energy* **2019**, *22*, 283–301.
44. Hayat, I.; Chatterjee, T.; Liu, H.; Peet, Y.T.; Chamorro, L.P. Exploring wind farms with alternating two- and three-bladed wind turbines. *Renewable Energy* **2019**, *138*, 764 – 774. doi:https://doi.org/10.1016/j.renene.2019.01.123.

45. Allaerts, D.; Meyers, J. Effect of inversion-layer height and Coriolis forces on developing wind-farm boundary layers. AIAA Paper 2016–1989, 2016. AIAA SciTech Forum/2018 Wind Energy Symposium, San Diego, CA.
46. Allaerts, D.; Meyers, J. Boundary-layer development and gravity waves in conventionally neutral wind farms. *Journal of Fluid Mechanics* **2017**, *814*. doi:doi:10.1017/jfm.2017.11.
47. Cava, D., K.; G.G., Scrimieri, A.; Poggi, D.; Cesatti, A.; U., G. Buoyancy and The Sensible Heat Flux Budget Within Dense Canopies. *Boundary-Layer Meteorol* **2011**, *118*, 217–240. doi:https://doi.org/10.1007/s10546-005-4736-1.
48. Banerjee, T.; De Roo, F.; Mauder, M. Connecting the Failure of K Theory inside and above Vegetation Canopies and Ejection–Sweep Cycles by a Large-Eddy Simulation. *Journal of Applied Meteorology and Climatology* **2017**, *56*, 3119–3131. doi:10.1175/JAMC-D-16-0363.1.
49. Wu, S.; Christensen, K.T.; Pantano, C. Modelling smooth- and transitionally rough-wall turbulent channel flow by leveraging inner–outer interactions and principal component analysis. *Journal of Fluid Mechanics* **2019**, *863*, 407–453. doi:10.1017/jfm.2018.899.
50. Peet, Y.; Fischer, P.; Conzelmann, G.; Kotamarthi, V. Actuator line aerodynamics model with spectral elements. AIAA Paper 2013–1210, 2013. 51st Aerospace Sciences Meeting, Grapevine, TX.
51. Mathis, R.; Monty, J.P.; Hutchins, N.; Marusic, I. Comparison of large-scale amplitude modulation in turbulent boundary layers, pipes, and channel flows. *Physics of Fluids* **2009**, *21*, 111703. doi:10.1063/1.3267726.
52. Ren, H.; Laima, S.; Li, H. Numerical study of amplitude modulation in the atmospheric boundary layer at very high Reynolds number. *AIP Advances* **2019**, *9*, 105112. doi:10.1063/1.5125566.
53. Perry, A.E.; Henbest, S.; Chong, M.S. Theoretical and Experimental studies of wall turbulence. *J. Fluid. Mech.* **1986**, *165*, 163–199.
54. Adrian, R.J. Hairpin vortex organization in wall turbulence. *Phys. Fluids* **2007**, *19*, 041301.
55. Tung, K.K.; Orlando, W.W. The k^{-3} and the $k^{-5/3}$ Energy Spectrum of Atmospheric Turbulence : Quasigeostrophic Two-Level model simulation. *Journal of Atmospheric Sciences* **2003**, *60*, 824–835.
56. Kraichnan, R.H. Inertial ranges of two-dimensional turbulence. *Phys. Fluids* **1967**, *10*, 1417–1423.
57. Brandt Belson, J.T.; Rowley, C. *Modred Library Documentation*, 2019.